

See discussions, stats, and author profiles for this publication at: <https://www.researchgate.net/publication/264462794>

Effect of Gas Adsorption on Acoustic Wave Propagation in MFI Zeolite Membrane Materials: Experiment and Molecular Simulation

ARTICLE in LANGMUIR · AUGUST 2014

Impact Factor: 4.46 · DOI: 10.1021/la502182k · Source: PubMed

CITATIONS

2

READS

64

9 AUTHORS, INCLUDING:



[Etoungh Dimitri Manga](#)

Université de Montpellier

13 PUBLICATIONS 28 CITATIONS

[SEE PROFILE](#)



[Philippe Da Costa](#)

Université de Montpellier

8 PUBLICATIONS 111 CITATIONS

[SEE PROFILE](#)



[Martin Drobek](#)

French National Centre for Scientific Research

35 PUBLICATIONS 226 CITATIONS

[SEE PROFILE](#)



[Emmanuel Le Clézio](#)

Université de Montpellier

50 PUBLICATIONS 358 CITATIONS

[SEE PROFILE](#)

Effect of Gas Adsorption on Acoustic Wave Propagation in MFI Zeolite Membrane Materials: Experiment and Molecular Simulation

Etoungh D. Manga,[†] Hugues Blasco,[†] Philippe Da-Costa,[†] Martin Drobek,[†] André Ayral,[†] Emmanuel Le Clezio,[‡] Gilles Despaux,[‡] Benoit Coasne,^{*,§,||,⊥} and Anne Julbe[†]

[†]Institut Européen des Membranes, UMR 5635-CNRS-ENSCM-UM2, University Montpellier 2, Place Eugène Bataillon, 34095 Montpellier, Cedex 5, France

[‡]Institut d'Electronique du Sud, UMR 5214-CNRS-UM2, University Montpellier 2, Place Eugène Bataillon, 34095 Montpellier, Cedex 5, France

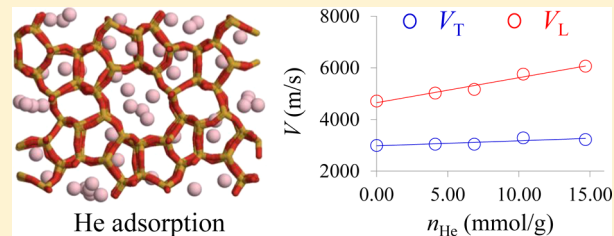
^{*}Institut Charles Gerhardt Montpellier, UMR 5253-CNRS-UM2-UM1-ENSCM, University Montpellier 2, Place Eugène Bataillon, 34095 Montpellier, Cedex 5, France

^{||}Department of Civil and Environmental Engineering, Massachusetts Institute of Technology, 77 Massachusetts Avenue, Cambridge, Massachusetts 02139, United States

[⊥]<MSE>, UMI 3466 CNRS-MIT, 77 Massachusetts Avenue, Cambridge, Massachusetts 02139, United States

S Supporting Information

ABSTRACT: The present study reports on the development of a characterization method of porous membrane materials which consists of considering their acoustic properties upon gas adsorption. Using acoustic microscopy experiments and atomistic molecular simulations for helium adsorbed in a silicalite-1 zeolite membrane layer, we showed that acoustic wave propagation could be used, in principle, for controlling the membranes *operando*. Molecular simulations, which were found to fit experimental data, showed that the compressional modulus of the composite system consisting of silicalite-1 with adsorbed He increases linearly with the He adsorbed amount while its shear modulus remains constant in a large range of applied pressures. These results suggest that the longitudinal and Rayleigh wave velocities (V_L and V_R) depend on the He adsorbed amount whereas the transverse wave velocity V_T remains constant.



1. INTRODUCTION

The study of ceramic membrane materials and processes is a rapidly expanding area due to the huge potential of membrane-based technology for both cost-effective environmentally progressive energy production and environmental pollution remediation systems.^{1,2} The performance of porous membranes and associated fluid transport properties are related to both their porous structure and the material characteristics.³ Both the bulk and surface physicochemical properties of the porous membrane material play important roles in transport mechanisms and can, to some extent, predict the interactions between different types of molecules on the material surface. The development of complex and sophisticated membrane designs down to the molecular scale created the need for a better insight into the relationships between the membrane synthesis route (a), material properties (b), microstructure (c), and transport properties (d). Information on membrane characteristics is essential for the users, manufacturers, and scientists to choose an appropriate material for a specific application, to control membrane synthesis process parameters, to evaluate membrane quality/stability (*ex situ* or *operando*), and also to favor the most relevant transport mechanism(s).

In order to further extend membrane applications to processes where safety constraints are extremely important (e.g., high temperature, high pressure conditions, toxic products, and/or corrosive atmospheres),^{4–6} the availability of reliable *online* diagnostic tools is essential to guarantee the membrane mechanical stability and integrity.

In this context, the acoustic emission (AE) is being considered as an attractive low-cost and fast nondestructive evaluation method which enables continuous *operando* control of materials (real time monitoring).⁷ If considering both surface (Rayleigh) and bulk (shear and compression) wave propagations, acoustic techniques are in fact well adapted to detect microstructure defects or changes in the mechanical properties of materials. However, to meet the requirements for an active membrane diagnostic tool based on acoustic measurements, a profound understanding of the membrane materials acoustic properties is required. In particular, the sensitivity of acoustic waves to gas adsorption and transport through porous membranes has never been reported in the literature and

Received: June 4, 2014

Revised: July 29, 2014

Published: August 4, 2014

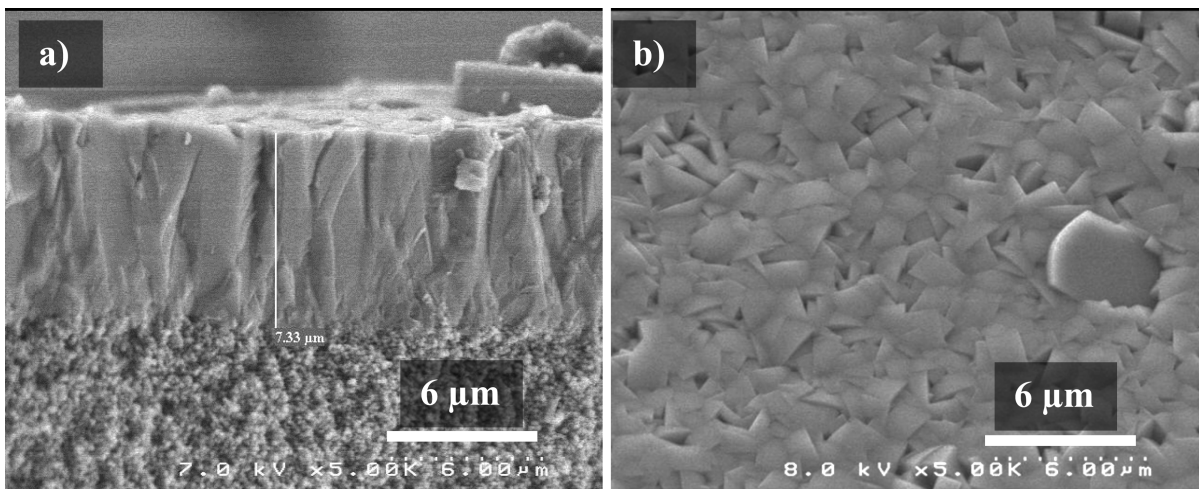


Figure 1. FESEM observation of the S-1 layer grown at 160 °C–12 h, from S-1 seeds deposited on α -Al₂O₃ porous disk: (a) cross-section view; (b) surface view.

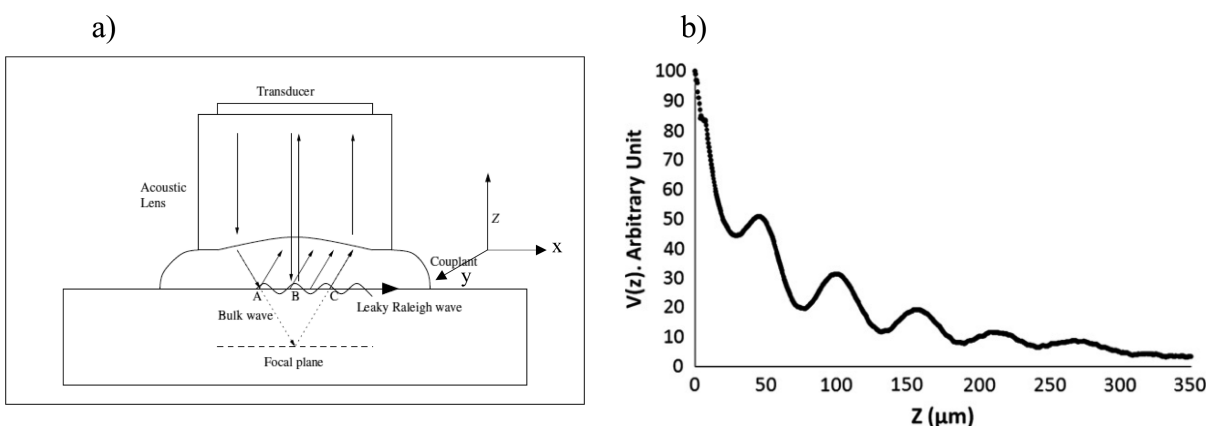


Figure 2. (a) Schematic representation of the scanning acoustic microscope (SAM). (b) Characteristic acoustic signature $V(z)$ for a supported thin layer.

must be established, in a relation with a model capable to predict the membrane and process performances during molecular transport of adsorbed species. Such a model must rely on a minimum set of simple physicochemical parameters, e.g., temperature and gas pressure enabling an estimation of elastic properties of the global system.⁸

Taking into account the above-mentioned assumptions, this paper reports a joint experimental and molecular simulation study of the effect of gas adsorption on the propagation of acoustic waves in a model, zeolite-based membrane. Zeolites are microporous materials with a well-defined porous structure and are relevant model systems to investigate the reciprocal influence of adsorption and mechanical properties.⁸ Silicalite-1 (S-1, MFI structure) was selected as a model material, which could be easily synthesized as a membrane (continuous thin layer on a porous support). Particular attention has been paid to computational and experimental methods including scanning acoustic microscopy (SAM) and both grand canonical Monte Carlo (GCMC) and molecular dynamics (MD) simulations, respectively, to investigate the effect of helium adsorption on the mechanical and acoustic properties of S-1 zeolite membrane. The comparison between as-obtained simulated and experimental results has been discussed in detail. While scanning acoustic microscopy and molecular simulations have been already applied separately to characterize materials, such

an approach combining molecular simulation and acoustic wave properties has not been published yet and might represent a significant asset for the *operando* characterization of porous membrane systems.

2. EXPERIMENTAL AND COMPUTATIONAL METHODS

2.1. Materials and Experimental Methods. **2.1.1. Ceramic Supports.** The silicalite-1 (S-1) zeolite layers were grown on porous α -Al₂O₃ ceramic disks (diameter = 25 mm, thickness = 1 mm) supplied by Fraunhofer-IKTS in Germany. These supports have an asymmetric structure composed of a thick macroporous substrate with 2.5 μm mean pore size and a thinner (thickness ~8 μm) top layer with 0.1 μm mean pore size.

2.1.2. Silicalite-1 Layer Synthesis. The MFI zeolite layers were prepared by a multistep procedure involving the secondary growth of S-1 seeds previously deposited on the above-described α -Al₂O₃ ceramic disks. For seed synthesis and secondary growth steps, two mother sols (1 and 2, respectively) were prepared by mixing tetraethyl orthosilicate (TEOS, 98%, Alfa Aesar), ultrapure water (18.2 MΩ), and tetrapropylammonium hydroxide (TPAOH, 1.0 M TPAOH aqueous solution, Alfa Aesar). S-1 seeds (50–100 nm) were prepared as reported previously,⁹ starting from mother sol 1 (molar composition: 1 SiO₂:0.4 TPAOH:19.5 H₂O:4 C₂H₅OH) and using a two-step MW-assisted hydrothermal protocol (first step at 80 °C for 90 min; second step at 125 °C for 60 min). An aqueous suspension of the derived S-1 nanoseeds (0.65 wt % S-1) was used to coat the α -Al₂O₃ ceramic disks with a thin S-1 layer. The supports were

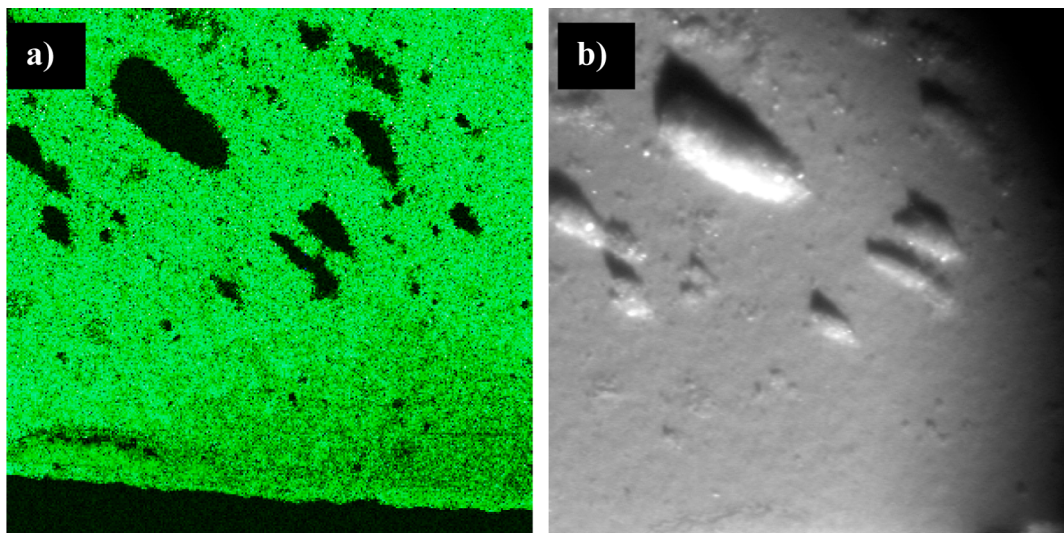


Figure 3. Images of the S-1 layer surface: (a) SAM-module imaging obtained with a 600 MHz ultrasonic sensor; (b) optical image obtained by using side lighting conditions. Both images correspond to a surface area of $3000\text{ }\mu\text{m} \times 3000\text{ }\mu\text{m}$.

repeatedly (3 times) immersed in the seed suspension (5 s contact time) and subsequently dried for 3 h at 150°C before being placed in an autoclave containing the secondary growth mother sol 2 (molar composition: 3 TPAOH:25 SiO₂:100 C₂H₅OH:1500 H₂O). The secondary growth step corresponds to a hydrothermal treatment with classical heating at 160°C for 12 h. After the synthesis, the supported zeolite layers were finally calcined in air at 550°C (heating rate $0.2^\circ\text{C}/\text{min}$, 4 h dwell time) and cooled down to room temperature ($0.4^\circ\text{C}/\text{min}$).

2.1.3. Characterization of the S-1 Zeolite Layers. The morphology, thickness, and homogeneity of membranes were studied at different locations by FESEM (Hitachi S-4500). The crystalline structure and crystal preferential orientation (CPO) in the membranes were examined by X-ray diffraction using Ni-filtered Cu K α radiation (XRD, PANalytical X-Pert Pro, 40 kV, 20 mA).

Figure 1 shows FESEM images of the MFI layers grown on the α -Al₂O₃ ceramic disks. The zeolite layers have a uniform thickness ($\sim 7\text{ }\mu\text{m}$) without any visible crack, delamination, or pinhole. Few isolated MFI zeolite crystals are randomly observed at the surface but do not alter membrane integrity. The crystal preferential orientation in the layer was oblique as confirmed by the observation of the (101) X-ray diffraction line. The resulting layer has a typical thickness in the range 5–10 μm .

An image of a $3000\text{ }\mu\text{m} \times 3000\text{ }\mu\text{m}$ area of the S-1 layer was recorded using high frequency scanning acoustic microscopy. The experimental setup is shown in Figure 2. Thanks to an acoustic lens, a scanning acoustic microscope (SAM) focuses ultrasonic waves issued from a transducer into the material or on its surface. Distilled water is used as coupling agent in order to ensure better contact between the transducer and the sample surface. (Silicalite-1 is an organophilic material so that it is unlikely that water penetrates the S-1 material during the SAM experiments which were conducted under atmospheric pressure and temperature.) The wave frequency is about 600 MHz, which yields a high spatial resolution of 2 μm . Moving the device in the x - y plane parallel to the material surface allows the reconstruction of qualitative acoustic images by assembling the signals reflected from the different locations. Quantitative estimation of the local material properties can be obtained by fixing x and y and scanning along the z -direction. This leads to the characteristic acoustic signature shown in Figure 2b. The observed oscillations are due to interactions between the longitudinal and surface waves whose velocities are related to the material properties.¹⁰

Using the high frequency SAM described above, 10 000 points images of the S-1 surface were recorded, and sound data corresponding to a 300-point line were used for statistical analysis of the zeolite membrane material properties. The longitudinal and

Rayleigh surface wave velocities derived from the acoustic signature were used to estimate the S-1 elastic properties such as Young modulus E , bulk modulus K , and shear modulus G .¹¹ More details about the experimental setup and acoustic wave measurements can be found elsewhere.¹⁰

2.2. Computational Details. **2.2.1. Models and Interaction Potentials.** Molecular simulation is an efficient technique which allows probing the thermodynamics and dynamics of systems at the microscopic scale. These simulations, which rely on statistical mechanics, provide ensemble averages of macroscopic properties.^{12,13} The simulation model of S-1 is a MFI-type structure (either orthorhombic with space group *Pnma* or monoclinic with space group *P21/n* at high and low temperature, respectively) and is characterized by a framework built of 4-, 5-, 6-, and 10-membered rings of SiO₄ tetrahedra forming channels with 5.5 Å mean pore diameters that are straight in the b -direction and sinusoidal in the xz -plane.^{14–16}

In all the simulations carried out in this work, the force field defined by Carré et al.,¹⁸ which was developed to describe bulk SiO₂, was used here to describe the interactions in S-1. In this model, the Si and O atoms, which carry a partial charge, interact through Coulombic interactions. In addition, they interact via Buckingham potentials which describe the repulsion and dispersion interactions. The He atoms were described using a Lennard-Jones potential with the parameters given in the literature.¹⁹ The cross interactions between He and Si atoms consist in a repulsion/dispersion interaction described using the Lennard-Jones potential. The cross-parameters for the Lennard-Jones potentials were obtained using the Lorentz–Berthelot combining rules (like atom parameters for silica and He are those given in refs 19 and 20, respectively). The electrostatic interaction was calculated using the Ewald sum to correct for the finite size of the simulation box. It should be emphasized that the interaction potentials used in the present work were not adjusted to reproduce the experimental data. As a result, the quantitative agreement between the simulated and experimental data (in terms of adsorption isotherms reported in Figure S1 and acoustic properties reported below) constitute a drastic test of the quality of the simulation techniques. Moreover, we note that the force fields used to model silica and helium have been demonstrated to reasonably capture the behavior of silica materials as well as the equation of state of helium.

2.2.2. Grand Canonical Monte Carlo (GCMC). Adsorption of He in S-1 at room temperature was investigated by means of GCMC simulations.⁸ In this technique, the system (S-1 + He) has a constant volume and is in equilibrium with a fictitious reservoir imposing its temperature T and chemical potential for helium μ_{He} . The calculations were performed for the orthorhombic phase of S-1, which corresponds to the stable structure at room temperature and for a pressure $P > 1$

GPa. However, we might note that the adsorption isotherm for the other MFI structure (ZSM-5) is very similar as its porous framework and pore volume are comparable.

2.2.3. Molecular Dynamics. For different amounts of He adsorbed in S-1 (obtained from the grand canonical Monte Carlo simulations described in the previous subsection), we measured the mechanical and acoustic properties of the composite system (S-1 + He) using molecular dynamics simulations. In this part of the work, we did not impose any structure for the S-1 framework as the latter was allowed to relax in the course of the simulation. In the molecular dynamics technique, the trajectory of the system is determined by numerically solving the Newton equation of motion for all atoms.¹⁷

3. RESULTS AND DISCUSSION

3.1. Scanning Acoustic Microscopy of the S-1 Zeolite Layer. The mechanical properties of the S-1 surface layer were derived from the experimental measurements, by SAM, of the longitudinal and Rayleigh wave velocities. These experimental results obtained with any He in the S-1 membrane layer will be useful to validate the theoretical ones derived from MD simulations of the S-1 material without any adsorbed gas. Colored images of a 3000 $\mu\text{m} \times 3000 \mu\text{m}$ area of the S-1 surface are shown in Figure 3. Figure 3a corresponds to the moduli of the recorded acoustic signals reflected from the material surface of during $x-y$ scan. This acoustic map reveals a nonuniform surface with green areas corresponding to flat regions in the focal plane of the transducer and dark areas corresponding to out-of-plane humps. This is consistent with the optical image shown in Figure 3b. The latter, which was obtained by using side lighting conditions, will be used in the following to infer the mechanical properties of the S-1 layer.

Regions where the surface appears to be uniform were selected in Figure 3a, and $V(z)$ measurements^{21,22} were performed at 300 locations of this uniform surface regions. The corresponding velocities are presented in Figure 4. Two

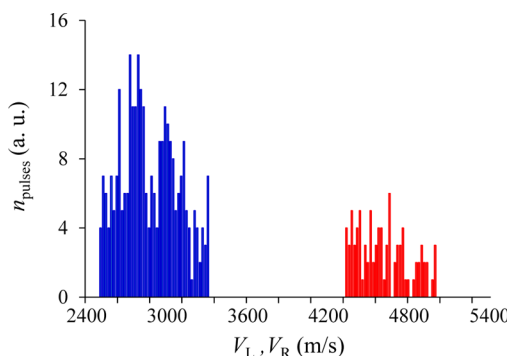


Figure 4. Distributions of longitudinal V_L (red) and Rayleigh V_R (blue) velocities measured at different locations of the S-1 film surface.

different modes can be clearly identified: a fast (respectively slow) mode with an average wave velocity of about 4600 ± 330 m/s (2870 ± 390 m/s) corresponding to the longitudinal wave velocity V_L (the Rayleigh wave velocity V_R).

The 7% (13%) error on V_L (V_R) is an indication of the material surface heterogeneity as mentioned in section 2.1. Indeed, the surface roughness observed in Figure 1b is of the order of the ultrasonic focal point which yields acoustic diffusion. This results in low signal-to-noise ratios in the recorded ultrasonic signals and leads to a high uncertainty on each velocity measurement. The homogeneous distribution of the measured velocities around their mean value can be linked

to acoustic effects rather than material inhomogeneity. As a result, the mean values should be regarded with a high degree of confidence as the actual standard deviation is only 190 m/s for V_L (210 m/s for V_R). The transverse wave velocity V_T can be determined by solving the following equation:¹¹ $V_R^6 - 8V_T^2V_R^4 + (24 - 16V_T^2/V_L^2)V_T^4V_R^2 + 16(V_T^2/V_L^2 - 1)V_T^6 = 0$. Then, the bulk K and shear G moduli are directly obtained by solving the following equations: $V_T = (G/\rho_{S-1})^{1/2}$ and $V_L = ((4G + 3K)/3\rho_{S-1})^{1/2}$. The experimental wave velocities found in the present work correspond to a Young modulus of 35.70 ± 2.55 GPa, a shear modulus $G_{\text{Voigt}} = 20.88 \pm 2.98$ GPa, and a bulk modulus $K_{\text{Voigt}} = 9.20 \pm 1.38$ GPa.

3.2. Molecular Simulation. Figure S1 in the Supporting Information shows the simulated He adsorption isotherm at 300 K in S-1 together with a typical configuration of the system. These simulated data, which were obtained using GCMC simulations, are in excellent agreement with the experimental data by Talu and Myers²⁴ (Figure S1). Our simulated data are also in good agreement with previous simulation data obtained by Skouidas and Sholl,²⁵ who used a different force field. These comparisons show that the force field used in the present work reasonably captures He adsorption and confinement in silicalite. The simulated adsorption isotherm obtained using GCMC simulations, which is of type I in the IUPAC classification, is typical of microporous solids (the mean pore diameter in S-1 is $D = 0.55$ nm).^{12,13} In agreement with the experimental data, we found that He adsorption in S-1 obeys the Henry law up to 500 kPa. Because of important thermal fluctuations at room temperature, the maximum adsorbed He amount (~ 30 mmol/g) is reached at very high pressures (10 GPa).

The mechanical and acoustic properties of S-1 loaded with different amounts of He were determined in the framework of Voigt formalism.²⁶ For each loading, we first determined the molecular energy of the *at equilibrium* structure by performing a molecular dynamics run at zero pressure in the NPT ensemble (constant number of molecules, pressure, and temperature). Starting from this *at equilibrium* configuration, we then considered the 21 possible deformations:

$$\mathbf{R}' = (\mathbf{I} + \boldsymbol{\epsilon})\mathbf{R} \quad (1)$$

where \mathbf{R} and \mathbf{R}' are the vector coordinates of each atom before and after the deformation. \mathbf{I} is the identity matrix while $\boldsymbol{\epsilon}$ is the 3×3 deformation matrix (corresponding to one of the 21 possible deformations). For each deformation mode, we considered the following 17 amplitudes δ [$-0.04, -0.035, -0.03, \dots, 0.03, 0.035, 0.04$]. For each deformation mode and amplitude, we performed a MD simulation run at constant deformation (NVT ensemble where the number of molecules, volume, and temperature of the system are kept constant) and estimated the average energy of the system.²⁷ As an example, Figure S2 in the Supporting Information shows the average energy of S-1 without any He atom, as a function of the deformation amplitude δ for the deformation mode consisting in expanding or contracting the system along the direction x . As expected, the evolution of the energy E of S-1 as a function of δ is parabolic with a minimum value corresponding to the minimum (unstrained) configuration. This result shows that the energy $E(\boldsymbol{\epsilon}_1)$ of the deformed configuration can be expressed as a second-order Taylor expansion around the minimum energy $E(0)$:

$$E(\epsilon_1) = E(0) + \frac{1}{2} \left(\frac{\partial^2 E}{\partial \epsilon_1^2} \right) \delta \quad (2)$$

A fit of the parabolic energy curve shown in Figure S2 allows estimating the elastic constant C_{11} :

$$E(\epsilon_1) = E(0) + \frac{1}{2} V C_{11} \delta^2 \quad (3)$$

From a general point of view, all the C_{ij} constants can be estimated using the same procedure applied to the 21 possible deformations.

Tables 1 and 2 show the simulated stiffness parameters C_{ij} and elastic properties of S-1 at 300 K and 0 GPa as obtained

Table 1. Simulated Stiffness Parameters C_{ij} Obtained Using MD Simulations (Determined from the Stiffness Parameters Using Voigt Formalism) of S-1 at 300 K and 0 GPa

I_j	C_{ij} (GPa)	I_j	C_{ij} (GPa)
11	45.46	66	14.45
22	54.11	12	-10.28
33	34.90	13	-2.49
44	18.13	23	-4.08
55	19.30		

Table 2. Simulated Properties Obtained Using MD Simulations (Determined from the Stiffness Parameters Using Voigt Formalism) of S-1 at 300 K and 0 GPa

property	value (error %)	property	value (error %)
ρ (g/cm ³)	1.75 (3)	V_L/V_T	1.57 (3)
K_{Voigt} (GPa)	13.44 (2)	ν	0.02 (3)
G_{Voigt} (GPa)	18.90 (3)	E (GPa)	38.15 (4)
V_L (m/s)	4714 (4)	V_R	2914 (5)
V_T (m/s)	2993 (3)		

using MD simulations. The value of the density ($\rho = 1.75$ g/cm³) is the exact value calculated from the S-1 framework (in good agreement with the S-1 mass density $\rho = 1.80$ g/cm³ reported in the literature²⁸). The bulk modulus K_{Voigt} , which is sometimes referred to as the incompressibility, is a measure of the ability of a substance to withstand changes in volume upon isotropic compression. K_{Voigt} can be estimated from the elastic constants C_{ij} using eq S1 given in the Supporting Information file. $K_{\text{Voigt}} = 13.44$ GPa is close to the value found in our previous work in which the energy versus volume curve for S-1 was fitted against the Birch–Murnaghan equation of state.⁸ This value is also in good agreement with the experimental values for S-1 (14 and 19 GPa at slow and fast compression, respectively).⁸ The shear modulus G_{Voigt} , also called the stiffness modulus, has a value of 18.90 GPa (G_{Voigt} can be estimated from the elastic constants C_{ij} using eq S2 given in the Supporting Information). This value, which is in the range of glass stiffness (26 GPa) and aluminum stiffness (25 GPa), is typical for zeolites.²⁹ The difference between the shear modulus ($G_{\text{Voigt}} = 18.90$ GPa) and bulk modulus ($K_{\text{Voigt}} = 13.44$ GPa) indicates that S-1 is difficult to deform under shear while it is relatively easy to deform under volume compression or expansion. The compressional wave velocity V_L and the shear wave velocity V_T can be deduced from K_{Voigt} and G_{Voigt} using the following equations:

$$V_T = \sqrt{\frac{G_{\text{Voigt}}}{\rho_{S-1}}} \quad (4)$$

$$V_L = \sqrt{\frac{4G_{\text{Voigt}} + 3K_{\text{Voigt}}}{3\rho_{S-1}}} \quad (5)$$

The Rayleigh wave velocity V_R ($V_R < V_T < V_L$), which results from interferences between longitudinal and transversal waves at a free surface, can be estimated as

$$\begin{aligned} V_R^6 - 8V_T^2V_R^4 + (24 - 16V_T^2/V_L^2)V_T^4V_R^2 \\ + 16(V_T^2/V_L^2 - 1)V_T^6 = 0 \end{aligned} \quad (6)$$

The derivation of eq 6, which can be found in refs 22 and 23, is obtained by solving the Navier equation for the dynamical equilibrium. The Young modulus E and Poisson ratio are also deduced from K_{Voigt} and G_{Voigt} :

$$E = \frac{9K_{\text{Voigt}}G_{\text{Voigt}}}{3K_{\text{Voigt}} + G_{\text{Voigt}}} \quad (7)$$

$$\nu = \frac{3K_{\text{Voigt}} - 2G_{\text{Voigt}}}{2(3K_{\text{Voigt}} + G_{\text{Voigt}})} \quad (8)$$

Earlier experimental studies have determined the Young modulus of S-1 crystal with very different results: $E \sim 4$, 38, and 79.6 GPa.^{30–32} We note that the experimental value $E = 79.6$ GPa was obtained for S-1 having a mass density of 2.04 g/cm³ which largely overestimates the nominal density of S-1. Several authors have also determined the Young modulus for S-1 layers: $E \sim 28$ and 41.8 GPa.^{33,34} Calculations based on the density functional theory (DFT) were also performed for high silica zeolites. The [100] axis was found to be the most rigid with $E = 162$ GPa while the [010] axis was found to be the softest with $E = 96$ GPa.³⁴ These authors concluded that the difference between these two directions stem from the high space group symmetry that was assumed in the calculation (such a high space symmetry was used to prevent crystal collapse). In the present work, we estimated the Young modulus from the compliance matrix S which is defined as the inverse of the stiffness matrix $C = [C_{ij}]$, i.e., $S = C^{-1}$. The Young modulus E_α in the direction $\alpha = x, y, z$ is directly obtained as $E_\alpha = 1/S_{\alpha\alpha}$.¹¹ Using this equation, we found $E_x = 42.9$ GPa, $E_y = 32.6$ GPa, and $E_z = 26.1$ GPa. These values, which are close from the value obtained by treating S-1 as an isotropic material $E = 38.15$ GPa (measured from the bulk and shear moduli using eq 7), show that the x - and y -directions in S-1 are stiffer than the z -direction. The Young moduli obtained from the MD simulations are in the range of the experimental value (35.70 GPa) obtained with scanning acoustic microscopy. Furthermore, treating S-1 as an isotropic material, we report a mean Poisson ratio $\nu = 0.02$. However, we note that this average value was obtained from a set of three MD simulations with two negative values and only one positive value. While further work is needed to clarify this issue (including better statistics), the two negative Poisson ratios suggest that S-1 exhibits auxetic behavior (i.e., negative Poisson ratio). This behavior results from a positive S_{12} compliance coefficient, indicating that the structure contracts along the transverse axis when compressed along the principal axis.³¹ The presence of the TPA template occupying most of the free-pore space might restrict the rotation of the tetrahedral framework units, therefore reducing

the flexibility of the structure and yielding the auxetic effect. The negative Poisson ratios are lower than those observed in the literature ($\nu = -0.5$ for α -cristobalite and $\nu = -0.12$ for natrolite MFI³⁵), which indicates that S-1 may possess a small auxetic behavior.

Figure 5 shows the unit cell volume V for S-1 as a function of the amount of adsorbed helium n_{He} (expressed in number of

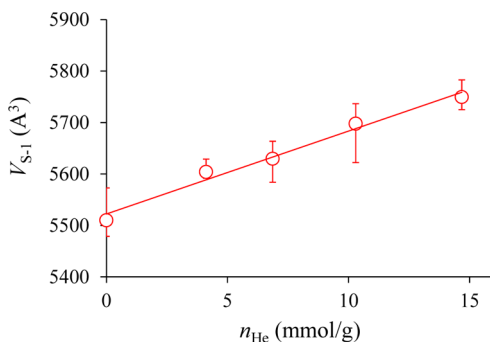


Figure 5. Unit cell volume V_{S-1} for S-1 loaded at 300 K with helium as a function of the adsorbed amount n_{He} (in mmol/g).

atoms per unit cell). For each adsorbed amount n_{He} , the unit cell volume was determined using a molecular dynamics run at zero pressure in the NPT ensemble (constant number of molecules, pressure, and temperature). In this ensemble, the pressure is fixed constant while the volume fluctuates around its equilibrium value V . In order to estimate the error bars on the data reported in the present work, for each adsorbed amount, all the mechanical calculations were performed for three initial configurations. These configurations, which were obtained in the course of the initial energy minimization step, have configurational energies very close to each other but correspond to slightly different atomic structures. The MD simulations have been performed for these three configurations, and the average result over the three sets of data is plotted in Figure 5. Starting from $V_{S-1} = 5510.1 \text{\AA}^3$ for $n_{\text{He}} = 0 \text{ mmol/g}$, V_{S-1} increases linearly up to 5725.1\AA^3 when n_{He} increases to 15 mmol/g (we recall that He adsorption obeys Henry's law in this range). As discussed above, the simulated initial volume for S-1 is in good agreement with the experimental value. The increase in the unit cell volume is due to the introduction of guest He atoms in S-1. A similar expansion of the S-1 volume has also been reported for CO_2 ⁸ and *n*-butane³⁶ adsorption (however, in the case of CO_2 , sample shrinkage was first observed upon adsorption of the first molecules).

In order to estimate the effect of He adsorption on the elastic properties of S-1, the evolutions of both K_{Voigt} and G_{Voigt} as a function of n_{He} are compared in Figure 6. K_{Voigt} increases linearly with increasing n_{He} . Starting from $K_{\text{Voigt}} = 13.44 \text{ GPa}$ for $n_{\text{He}} = 0 \text{ mmol/g}$, K_{Voigt} increases up to 38.28 GPa as n_{He} increases to 15 mmol/g. This shows that even a relatively small n_{He} amount alters the mechanical behavior of S-1 by increasing K_{Voigt} by $\sim 110\%$. This result is in full agreement with our previous work on CO_2 in zeolites in which it was shown that the mechanical properties of microporous solids are enhanced by adsorption of guest species.⁸ In contrast, the shear modulus G_{Voigt} is nearly insensitive to n_{He} and remains constant at about 17.2 GPa. We emphasize that the properties determined according to the above procedure correspond to undrained conditions since He was not allowed to flow out from the sample. Since we are mainly interested in determining the effect

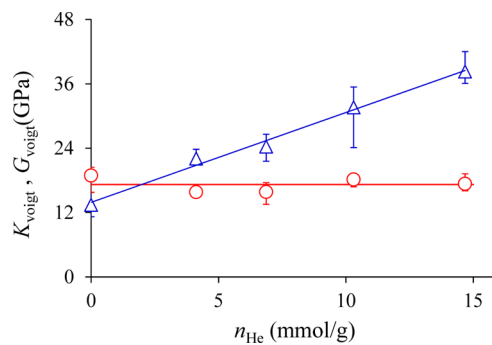


Figure 6. Simulated elastic properties G_{Voigt} (red circles) and K_{Voigt} (blue triangles) of S-1 as a function of n_{He} (obtained using MD simulations). These data correspond to the values averaged over three different initial configurations. The data for each configuration can be found in Figure S3 of the Supporting Information.

of He atoms passing through the zeolite sample on its acoustic properties, the latter condition is sufficient. In contrast, a poromechanical approach must be used if one wants to look at the effect of adsorption on the sample mechanical deformation.³⁷

For each adsorbed amount n_{He} , the compressional wave velocity V_L and shear wave velocity V_T were calculated from the bulk and shear moduli according to eqs 4 and 5. V_L and V_T are shown in Figure 7 as a function of n_{He} . While $V_T = 3118 \pm 93$

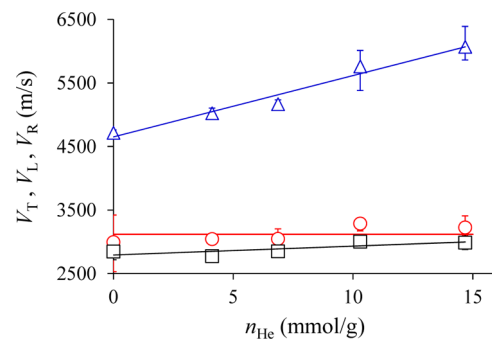


Figure 7. Simulated acoustic velocities V_T (red circles), V_L (blue triangles), and V_R (black squares) of S-1 as a function of n_{He} (obtained using MD simulations). These data correspond to the values averaged over three different initial configurations. The data for each configuration can be found in Figure S4 of the Supporting Information.

m/s remains constant, V_L increases when increasing the amount of adsorbed helium n_{He} . The compressional velocity V_L increases linearly from 4714 ± 188 to 6067 ± 242 m/s when n_{He} increases from 0 to 15 mmol/g. As previously shown, the acoustic velocities are useful for investigating the mechanical changes occurring in materials.³⁷ The simulated longitudinal wave velocity in the absence of any adsorbed He is in very good agreement with the value measured by SAM experiments $V_L = 4600 \pm 330$ m/s.

In *operando* devices, samples are embedded in the system so that it is often impossible to perform bulk wave measurements as only one free surface is available. By only measuring the surface wave velocity V_R , scanning acoustic microscopy allows one to assess both E and G . Indeed, for the evaluation of V_R , only one free surface is needed. If the Poisson ratio ν is known, V_T and V_L can be calculated using the experimental value of V_R so that E and G are easily deduced.^{21,22} These mechanical

properties will be useful data for the implementation of acoustic methods as new tools for the qualitative description of *operando* membranes properties and transport mechanisms; this will be the next step of this preliminary work.

In order to determine the effect of adsorption on the Rayleigh wave propagation, Figure 7 also shows V_R which was estimated from eq 6. At 300 K and 0 GPa, the simulated Rayleigh wave velocity was found to be equal to 2914 ± 145 m/s. By comparing this theoretical value with that obtained by SAM experiments, the agreement is very good since these two values differ by only 1.3% ($V_R = 2870 \pm 390$ m/s in the experiments). Given that V_R depends both on the compressional wave velocity V_L and on the shear wave velocity V_T , it increases with increasing the adsorbed amount n_{He} .

4. CONCLUSION

This paper is a first step toward the development of an *operando* characterization of porous membranes by means of focused acoustic microscopy combined with atom-scale simulation. We have shown that simple molecular simulations of gas adsorption can be used to predict the mechanical and acoustic behavior of zeolites depending on the applied pressure. This approach allows one to accurately relate the macroscopic mechanical and acoustic properties such as compressional and shear moduli to the atomic structure in a composite system made of S-1 zeolite and gas. This simulation strategy was validated by comparing with experimental data obtained from high frequency acoustic microscopy. The experimental longitudinal and surface wave velocities are in good agreement with those obtained by means of molecular simulation. Combining molecular simulation and acoustic wave properties is an asset to monitor in real time, i.e., *operando*, the evolution of the mechanical properties of porous media and membranes. In particular, starting from an established set of acoustic properties for a given undeteriorated membrane material under normal working conditions, any measured deviations of the scanning acoustic microscopy results can be considered as a potential source of defects in the membrane film. As a result, such an *operando* characterization technique would provide both a checking procedure of the working conditions of a given membrane and a means to detect possible deterioration of the setup.

While other efficient methods for detecting cracks in membranes are available (such as IR spectroscopy, X-ray microtomography, and electric resistance tomography), scanning acoustic microscopy possesses several advantages which makes this technique, if successful, very powerful and attractive. First, considering that scanning acoustic microscopy is based on ultrasound propagation, it is very sensitive to the mechanical-elastic behavior of materials at scales corresponding to the wavelength, i.e., \sim micrometers. It is therefore suitable to characterize materials and their heterogeneity and to detect possible defects. Moreover, such an acoustic method enables nondestructive control of the materials and could thus be considered as a step toward *in situ* monitoring of damage formation/evolution during membrane operation. In theory, this technique could be applied to any types of membranes including inorganic membranes such as ceramic membranes as well as organic membranes such as polymer membranes. However, owing to their “softer” nature, the acoustic response for organic membranes can be much more difficult to analyze using acoustic microscopy. Moreover, the swelling of organic membranes such as polymers in contact with gas phases is a

complex problem which has to be considered in further investigation. While poromechanical models are available in the literature to describe the changes in porous volume and unit cell upon gas adsorption,^{37,38} combining such models with acoustic microscopy is a difficult task which requires further work. As a result, our intention is to first apply the method to microporous ceramic and hybrid membranes such as zeolites and MOFs before considering more complex materials such as polymer membranes.

■ ASSOCIATED CONTENT

§ Supporting Information

Additional data including He adsorption isotherm in MFI. This material is available free of charge via the Internet at <http://pubs.acs.org>.

■ AUTHOR INFORMATION

Corresponding Author

*E-mail: coasne@mit.edu (B.C.).

Author Contributions

E.D.M. and H.B. contributed equally to this work.

Notes

The authors declare no competing financial interest.

■ ACKNOWLEDGMENTS

The authors acknowledge the financial support of both the European Commission (CARENA project - FP7-NMP-2010-LARGE, GA No. 263007) and the LabEx CheMISyst at the University Montpellier 2 (COM-EA project-TZ/DN 12-29).

■ REFERENCES

- (1) Bose, A. C. *Inorganic Membranes for Energy and Environmental Applications*; Springer: Berlin, 2009.
- (2) Li, K. *Ceramic Membranes for Separation and reaction*; Wiley-VCH: Weinheim, 2007.
- (3) Mallada, R.; Menéndez, M. *Inorganic Membranes: Synthesis, Characterization and Applications*; European Membrane Society; Elsevier: Amsterdam, 2008.
- (4) Hu, Y.; Yan, J. Characterization of flue gas in oxy-coal combustion processes for CO₂ capture. *Appl. Energy* **2012**, *90*, 113–121.
- (5) Favre, E. Carbon dioxide recovery from post-combustion processes: Can gas permeation membranes compete with absorption? *J. Membr. Sci.* **2007**, *294*, 50–59.
- (6) Yang, T.; Chung, T. S. High performance ZIF-8/PBI nanocomposite membranes for high temperature hydrogen separation consisting of carbon monoxide and water vapor. *Int. J. Hydrogen Energy* **2012**, *38*, 229–239.
- (7) Bruneau, M.; Potel, C. *Matériaux et acoustique 3: caractérisation des matériaux, contrôle non destructif et applications médicales*; Hermès Science Publ.: Lavoisier-Paris, 2006.
- (8) Coasne, B.; Haines, J.; Levelut, C.; Cambon, O.; Santoro, M.; Gorelli, F.; Garbarino, G. Enhanced mechanical strength of zeolites by adsorption of guest molecules. *Phys. Chem. Chem. Phys.* **2011**, *13*, 20096–20099.
- (9) Motuzas, J.; Julbe, A.; Noble, R. D.; Guizard, C.; Beresnevicius, Z. J.; Cot, D. Rapid synthesis of silicalite-1 seeds by microwave assisted hydrothermal treatment. *Microporous Mesoporous Mater.* **2005**, *80*, 73–83.
- (10) Briggs, G. A. D.; Kolosov, O. V. *Acoustic Microscopy*, 2nd ed.; Oxford University Press: Oxford, 2009.
- (11) Dieulestant, E.; Royer, D. *Elastic Waves in Solids I, Free and Guided Propagation*; Springer-Verlag: Berlin, 2000; p 155.

- (12) Coasne, B.; Galarneau, A.; Pellenq, R. J. M.; Di Renzo, F. Adsorption, intrusion and freezing in porous silica: the view from the nanoscale. *Chem. Soc. Rev.* **2013**, *42*, 4141–4171.
- (13) Coasne, B.; Ugliengo, P. Atomistic model of micelle-templated mesoporous silicas: structural, morphological and adsorption properties. *Langmuir* **2012**, *28*, 11131–11141.
- (14) Baerlocher, C.; McCusker, L. B. Database of zeolite structures: <http://www.iza-structure.org/databases/>.
- (15) Olson, D. H.; Kokotailo, G. T.; Lawton, S. L.; Meier, W. M. Crystal structure and structure-related properties of ZSM-5. *J. Chem. Phys.* **1981**, *85*, 2238–2243.
- (16) Hay, D. G.; Jaeger, H. J. Orthorhombic-monoclinic phase changes in ZSM-5 zeolite/silicalite. *J. Chem. Soc., Chem. Commun.* **1984**, 1433.
- (17) Alder, B. J.; Wainwright, T. E. Studies in molecular dynamics. I. General method. *J. Chem. Phys.* **1959**, *31*, 459–466.
- (18) Carre, A.; Horbach, J.; Ispas, S.; Kob, W. New fitting scheme to obtain effective potential from Car-Parrinello molecular dynamics simulations: Application to silica. *Eur. Phys. Lett.* **2008**, *82*, 17001–17006.
- (19) Lee, S. H.; Rossky, P. J. A comparison of the structure and dynamics of liquid water at hydrophobic and hydrophilic surfaces - a molecular dynamics simulation study. *J. Chem. Phys.* **1994**, *100*, 3334–3345.
- (20) Hirschfelder, J. O.; Curtiss, C. F.; Bird, R. B. *Molecular Theory of Gases and Liquid*; John Wiley and Sons, Inc.: New York, 1954.
- (21) Da Fonseca, R. J. M.; Ferdj-Allah, L.; Despaux, G.; Boudour, A.; Robert, L.; Attal, J. Scanning acoustic microscopy - Recent applications in materials science. *Adv. Mater.* **1993**, *5*, 7–8.
- (22) Laux, D.; Baron, D.; Despaux, G.; Kellerbauer, A. I.; Kinoshita, M. Determination of high burn-up nuclear fuel elastic properties with acoustic microscopy. *J. Nucl. Mater.* **2012**, *420*, 94–100.
- (23) Deladerriere, N.; Delaye, J. M.; Augereau, F.; Despaux, G.; Peuget, S. Molecular dynamics study of acoustic velocity in silicate glass under irradiation. *J. Nucl. Mater.* **2008**, *375*, 120–134.
- (24) Talu, O.; Myers, A. L. Molecular simulation of adsorption: Gibbs dividing surface and comparison with experiment. *AIChE J.* **2001**, *45*, 1160–1168.
- (25) Skouidas, A. I.; Sholl, D. S. Transport diffusivities of CH₄, CF₄, He, Ne, Ar, Xe, and SF₆ in silicalite from atomistic simulations. *J. Phys. Chem. B* **2002**, *106*, 5058–5067.
- (26) Voigt, W. *Lehrbuch der Kristallphysik*; Teubner Verlag: Berlin, 1928.
- (27) Hantal, G.; Brochard, L.; Laubie, H.; Ebrahimi, D.; Pellenq, R. J.-M.; Ulm, F.-J.; Coasne, B. Atomic-scale modelling of elastic and failure properties of clays. *Mol. Phys.* **2014**, *112*, 1294–1305.
- (28) Szostak, R. *Molecular Sieves: Principles of Synthesis and Identification*; Van Nostrand Reinhold: New York, 1989.
- (29) Crandall, S. H.; Dahl, N. C.; Lardner, T. J. *An Introduction to the Mechanics of Solids*; McGraw-Hill: Boston, 1959.
- (30) Wang, Z.; Lobo, R. F.; Lambros, J. The mechanical properties of siliceous ZSM-5 (MFI) crystals. *Microporous Mesoporous Mater.* **2003**, *57*, 1–7.
- (31) Sanchez-Valle, C.; Lethbridge, Z. A. D.; Sinogeikin, S. V.; Williams, J. J.; Walton, R. I.; Evans, K. E.; Bass, J. D. Negative Poisson's ratios in siliceous zeolite MFI-silicalite. *J. Chem. Phys.* **2008**, *128*, 184503–184505.
- (32) Brabec, L.; Bohac, P.; Stranyanek, M.; Ctvrtlik, R.; Kocirik, M. Hardness and elastic modulus of silicalite-1 crystal twins. *Microporous Mesoporous Mater.* **2006**, *94*, 226–233.
- (33) Baimpos, T.; Nikolakis, V.; Kouzoudis, D. Measurement of the elastic properties of zeolite films using Metglas-zeolite composite sensors. *Stud. Surf. Sci. Catal.* **2008**, *174*, 665–668.
- (34) Li, Z.; Johnson, M. C.; Sun, M.; Ryan, E. T.; Earl, D. J.; Maichen, W.; Martin, J. I.; Li, S.; Lew, C. M.; Wang, J.; Deem, M. W.; Davis, M. E.; Yan, Y. Mechanical and dielectric properties of pure-silica-zeolite low-k materials. *Angew. Chem., Int. Ed.* **2006**, *45*, 6329–6332.
- (35) Grima, J. N.; Jackson, R.; Alderson, A.; Evans, K. E. Do zeolites have negative Poisson's ratios? *Adv. Mater.* **2000**, *12*, 1918.
- (36) Sorenson, S. G.; Smyth, J. R.; Kocirik, M.; Zikanova, A.; Noble, R. D.; Falconer, J. L. Adsorbate-induced expansion of silicalite-1 crystals. *Ind. Eng. Chem. Res.* **2008**, *47*, 9611–9616.
- (37) Brochard, L.; Vandamme, M.; Pellenq, R. J. M. Poromechanics of microporous media. *J. Mech. Phys. Solids* **2012**, *60*, 606–622.
- (38) Coudert, F. X.; Boutin, A.; Fuchs, A. H.; Neimark, A. V. Adsorption deformation and structural transitions in metal–organic frameworks: From the unit cell to the crystal. *J. Phys. Chem. Lett.* **2013**, *4*, 3198–3205.